Ongoing Persistent Slope Failures at the Toe of a Giant Submarine Slide in the Ryukyu Trench that Generated the AD 1771 Meiwa Tsunami

Kiichiro Kawamura, Kazumasa Oguri, Mutsuo Inoue, Kan-Hsi Hsiung, Taishi Kudaka, and Ken Takai

Abstract

This study investigates sedimentation processes and associated submarine sliding on the floor of the Ryukyu Trench. Three dive surveys were conducted using the manned submersible *Shinkai 6500* (hereafter 6K) in the trench. The AD 1771 Meiwa tsunami was generated by a giant submarine slide on the landward trench slope in this region. Dive survey site 6K#1469 was located on a mouth of the submarine canyon in the forearc basin. Dive survey site 6K#1468 was located on the uppermost part of the submarine slide, where steps and fissures were observed. Dive survey site 6K#1467 was located at the toe of the submarine slide, which is covered by a muddy sediment layer. Core sample 6K#1467 measured 36.3 cm long and comprised muddy sediments interlayered with silt and/or sand laminations. The paleocurrent direction of the laminated sediments is mostly from north to south, indicating that they were not transported along with the trench but were from the landward slope, probably via repeated small submarine slides. The sedimentation rate for sample 6K#1467 was estimated at 2.42 mm/year using a depth profile of $^{210}Pb_{ex}$ concentration within 10 cm deep and a date for the sediment of ~ 50 year ago. Based on the sedimentation rate and the number of laminae, the typical recurrence interval of the silt/sand layers is calculated to be ~ 6 year. We interpret these results as indicating that repeated small submarine slides have occurred persistently (recurrence interval of ~ 6 year) at the toe of the investigated giant submarine slide in the Ryukyu Trench over the last 50 year.

Keywords

Submarine slide • *Shinkai 6500* • ITRAX • ^{210}Pb • Paleocurrent • Ryukyu Trench

K. Kawamura (✉)
Graduate School of Science and Technology for Innovation, Yamaguchi University, 1677-1 Yoshida, Yamaguchi-City, Yamaguchi, 753-8512, Japan
e-mail: kiichiro@yamaguchi-u.ac.jp

K. Oguri
HADAL and Nordcee, Department of Biology, University of Southern Denmark, Campusvej 55, 5230 Odense M, Denmark
e-mail: ogurik@biology.sdu.dk

K. Oguri
Research Institute for Global Change (RIGC), JAMSTEC, 2-15 Natsushima-cho, Yokosuka-City, Kanagawa, 237-0061, Japan

M. Inoue
Low Level Radioactivity Laboratory, Institute of Nature and Environmental Technology, Kanazawa University, Nomi, Ishikawa, 923-1224, Japan
e-mail: i247811@staff.kanazawa-u.ac.jp

K.-H. Hsiung
Research Institute for Marine Geodynamics (IMG), JAMSTEC, 2-15 Natsushima-cho, Yokosuka-City, Kanagawa, 237-0061, Japan
e-mail: hsiung@jamstec.go.jp

T. Kudaka
Faculty of Science, Yamaguchi University, 1677-1 Yoshida, Yamaguchi-City, Yamaguchi, 753-8512, Japan

K. Takai
Institute for Extra-Cutting-Edge Science and Technology Avant-Garde Research (X-Star), JAMSTEC, 2-15 Natsushima-cho, Yokosuka-City, Kanagawa, 237-0061, Japan
e-mail: kent@jamstec.go.jp

1 Introduction

Numerous coralline and reef boulders are considered to have been deposited by paleo-tsunamis on the Sakishima Islands at the southeastern end of Japan (Goto et al., 2010; Hisamitsu et al. 2014). Araoka et al. (2013) reported that eight tsunamis have struck the Sakishima Islands during the last ~ 2400 year (250 ± 100 BC, AD 200 ± 100, AD 550 ± 100, AD 800 ± 100, AD 1100 ± 100, AD 1400 ± 100, AD 1600 ± 100, and AD 1800 ± 100), as inferred from radiocarbon dating of 92 *Porites* boulders. The latter two events are consistent with historically recorded

I. Alcántara-Ayala et al. (eds.), *Progress in Landslide Research and Technology, Volume 1 Issue 2, 2022*, Progress in Landslide Research and Technology,
https://doi.org/10.1007/978-3-031-18471-0_5

events that occurred in 1625 and 1771, respectively (Araoka et al. 2013; Hisamitsu et al. 2014).

The giant 1771 Yaeyama tsunami (or 1771 Meiwa tsunami) resulted in runups of up to 30 m and 12,000 deaths on the Sakishima Islands in the southwestern Ryukyu Arc (Nakamura et al. 2009; Okamura et al. 2018). Nakamura et al. (2009) proposed that this tsunami was caused by an earthquake of moment magnitude (Mw) 8.0 that occurred in subducted sediments beneath the accretionary wedge. However, Okamura et al. (2018) reported that a submarine slide on the accretionary prism is a plausible source of the 1771 tsunami, based on a simple simulation and seismic survey results.

Most such submarine slides occur on the hanging wall of active thrust faults (Kawamura et al. 2009; Yamada et al. 2009), whereby the hanging wall is thrust upward during fault motion which subsequently collapses to initiate a submarine slide. A submarine slide results from slope instability caused by steepening of the hanging wall through cumulative thrust motion. The thrust events might be recorded in downslope basins as submarine slide deposits.

In this study, we investigate the sedimentation processes of turbidite layers in the Ryukyu Trench floor. Our results show that these layers have resulted from repeated small submarine slides originating from the landward trench slope that are caused by small collapse of the hanging wall of the frontal thrust. The recurrence interval of the slides is calculated roughly at $\sim$ 6 year. We conclude that the hanging wall of the frontal thrust has collapsed by repeated retrogressive submarine slides for at least $\sim$ 50 year ago.

2 Tsunamigenic Submarine Slides

Submarine slides are generally formed by source area, main track and depositional area (Fig. 1). The source and depositional areas are formed by extensional and compressional deformations, so that these are characterized by subsidence and uplifting, respectively. These seabed vertical motions could generate a tsunami. The size of the tsunami wave would not only be controlled by its geological architecture, but also by deformation speed, physical and mechanical properties of seabed materials and water depth of the submarine slides (Kawamura et al. 2017).

There are many historical accounts of tsunamigenic submarine slides. We briefly introduce the representative recent historical examples except for the 1777 Meiwa tsunami mostly following Kawamura et al. (2014).

The Lisbon earthquake of around Mw 8.5 occurred on November 1, 1755 on the Sao Vincentre Fault, off the coast of Portugal. Large tsunamis devastated Lisbon and other North Atlantic coasts both in Europe and Africa. Gracia et al. (2003) showed the probability for tsunamis genesis partly by submarine slides on the hanging wall of the thrust fault.

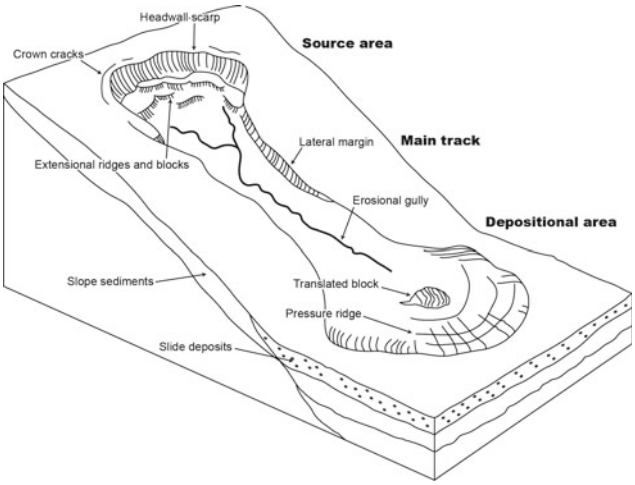

Fig. 1 General topography and internal structure of submarine slides (After Kawamura 2020)

On March 27, 1964, a moment magnitude Mw 9.2 earthquake generated large tsunamis of tsunami magnitude (Mt) 9.1 in Alaska (Abe 1979). Plafker and Mayo (1965) described localized tsunami waves excited by submarine slides that occurred in river deltas, terminal moraines, and so on. The tsunamis were approximately 3.0–4.5 m high and hit many bay areas about 19–20 min after the earthquake.

On June 15, 1896, the Meiji Sanriku earthquake generated devastating tsunamis with a maximum run-up of 37 m, and caused the worst tsunami disaster in Japanese history, despite having a surface wave magnitude (Ms) of only 7.2 and a low seismic intensity (Tanioka and Satake 1996). Abe (1979) showed that in spite of the low Ms, the Mt of this event was up to 8.6. To explain the discrepancy between Ms and Mt, the 1896 Sanriku earthquake has been variously attributed to slow rupture along the fault (Kanamori 1972), submarine slides (Kanamori and Kikuchi 1993), and additional rapid uplift of a sediment wedge (Tanioka and Seno 2001). Kawamura et al. (2012; 2014) supported the submarine slide scenario on the basis of topographic analysis and the geologic architecture.

On 1 April, 1946, Ms 7.1 earthquake occurred and generated large tsunamis (Mt = 9.3) along the Alaskan coastline that killed 167 people. Fryer et al. (2004) suggested that these tsunamis resulted from submarine slides (the Ugamak Slide), with head scars at water depths of approximately 200 m in the coastal area.

On 17 July, 1998, tsunamis with maximum wave heights of 15 m inundated Sissano in Papua New Guinea following Mw 7.1 earthquake (Kawata et al. 1999). Based on detailed seafloor mapping data, Tappin et al. (2001, 2008) concluded that the large tsunami was caused by a submarine slide

located offshore from the lagoon. This tsunami was rapidly excited by the earthquake (Newman and Okal 1988), but it was generated by subsequent submarine slides (2008).

On 12 January, 2010, the Haiti earthquake (Mw = 7.0) exhibited a primarily strike–slip motion, it nevertheless generated a tsunami (Hornbach et al. 2010). The earthquake caused liquefaction in several river deltas, which prograded rapidly and were prone to failure. It was concluded that the earthquake initiated a slide-generated tsunami along the shoreline.

Similar tsunamis occurred at Bay of Palu, induced by an earthquake in Sulawesi Island of Indonesia on 28 September, 2018 (Mw = 7.5) (Sassa and Takagawa 2019). These were excited by submarine slides along the bay due to liquefaction of coastal regions (Sassa and Takagawa 2019). Maximum run-up height was 11.3 m and average inundation distance was ∼ 200 m (Sassa and Takagawa 2019). The number of casualties was 2000 and the number of missing persons exceeds 5000.

In summary, all of these historical examples of tsunamis induced by submarine slides and/or presumable ones were excited by earthquake activity. These examples strongly suggested that the preconditioning factors on submarine slopes play an important role in excitation of the tsunamigenic submarine landslides. Therefore, understanding the preconditioning factors, not only using monitoring systems, but also using topographic analyses are significant to reduce the loss of the lives by tsunamis. Size and frequency of small submarine landslides could demonstrate the state of the slope stability.

3 Detailed Bathymetry and Dive Surveys

The landward trench slope of the southwestern Ryukyu Arc is composed of a steep upper slope, forearc basin, and accretionary prism from north to south (Okamura et al. 2018; Fig. 2). These forearc structures west of 122° 40′ E have been disrupted owing to tectonic movements related to arc–continent collision at Taiwan, back-arc rifting of the Okinawa Trough, and the high subduction obliquity of the Philippine Sea Plate (PSP), which contains ridges and seamounts (Okamura et al. 2018) and is converging with the Amur plate at a rate of 62–72 mm/year (Seno et al. 2005). At the Amur plate, the prism has been sliding to the west, relative to the arc, along dextral strike-slip faults that are clearly imaged by bathymetric mapping along the landward prism margin (Okamura et al. 2018; Fig. 2). The fault motion is interpreted to have been caused by slip-partitioning of the oblique subduction of the PSP (Okamura et al. 2018).

We conducted three dive surveys using the manned submersible *Shinkai 6500* (hereafter 6K) in the Ryukyu Trench region during cruise YK16-11 by the vessel

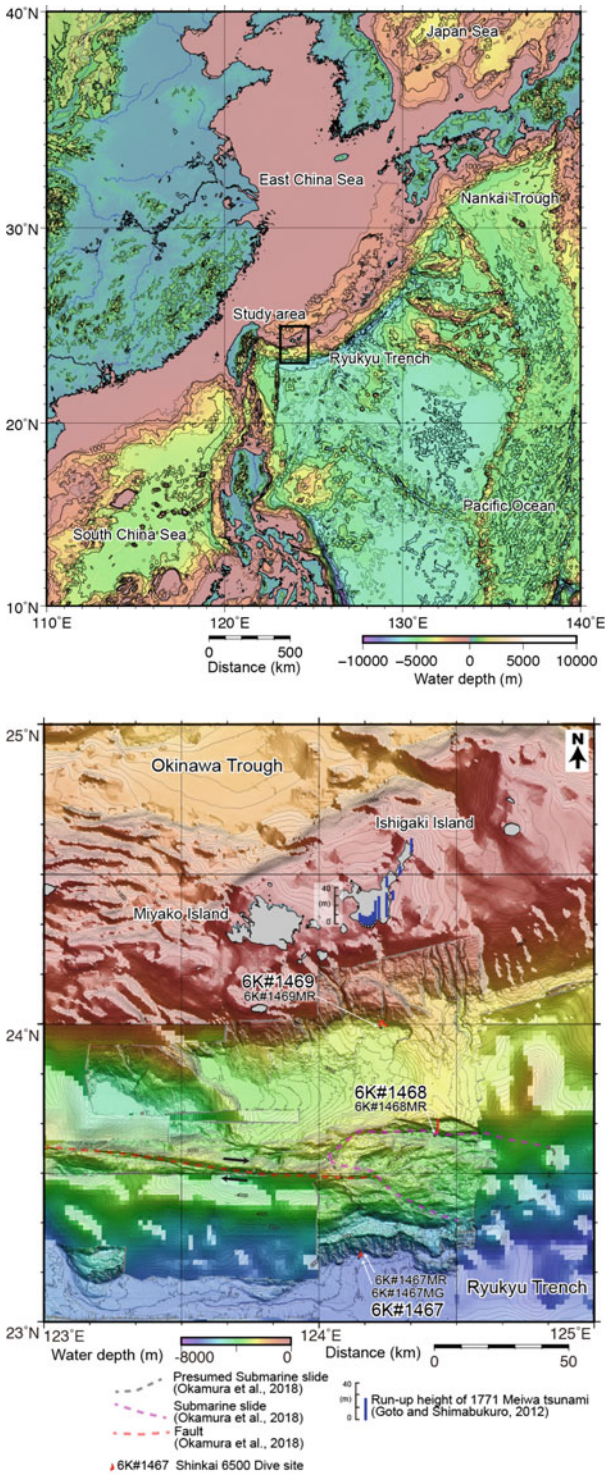

Fig. 2 Detailed topography and bathymetry in the study area. Upper shows location of the study area (black square) using ETOPO1, and lower shows dive locations using bathymetric survey data. Red lines indicate the dive routes followed during surveys from the *Shinkai 6500* vessel: 6K#1467, 6K#1468, and 6K#1469. Blue bars around Ishigaki Island show the run-up height of the AD 1771 Meiwa Tsunami (after Goto and Shimabukuro 2012). Broken lines demarcate the outline of the presumed submarine slide (gray), the submarine slide (pink), and the fault (red) identified by seismic surveys

Yokosuka. The dive surveys are referred as 6K#1467, 6K#1468, and 6K#1469 (Figs. 2 and 3). Survey 6K#1467 was performed on 1 September 2016 on the Ryukyu Trench floor at the foot of the landward trench slope. On the lower slope at a water depth of 6350 m, we collected a sediment core sample from the flat seafloor (sample 6K#1467MG)

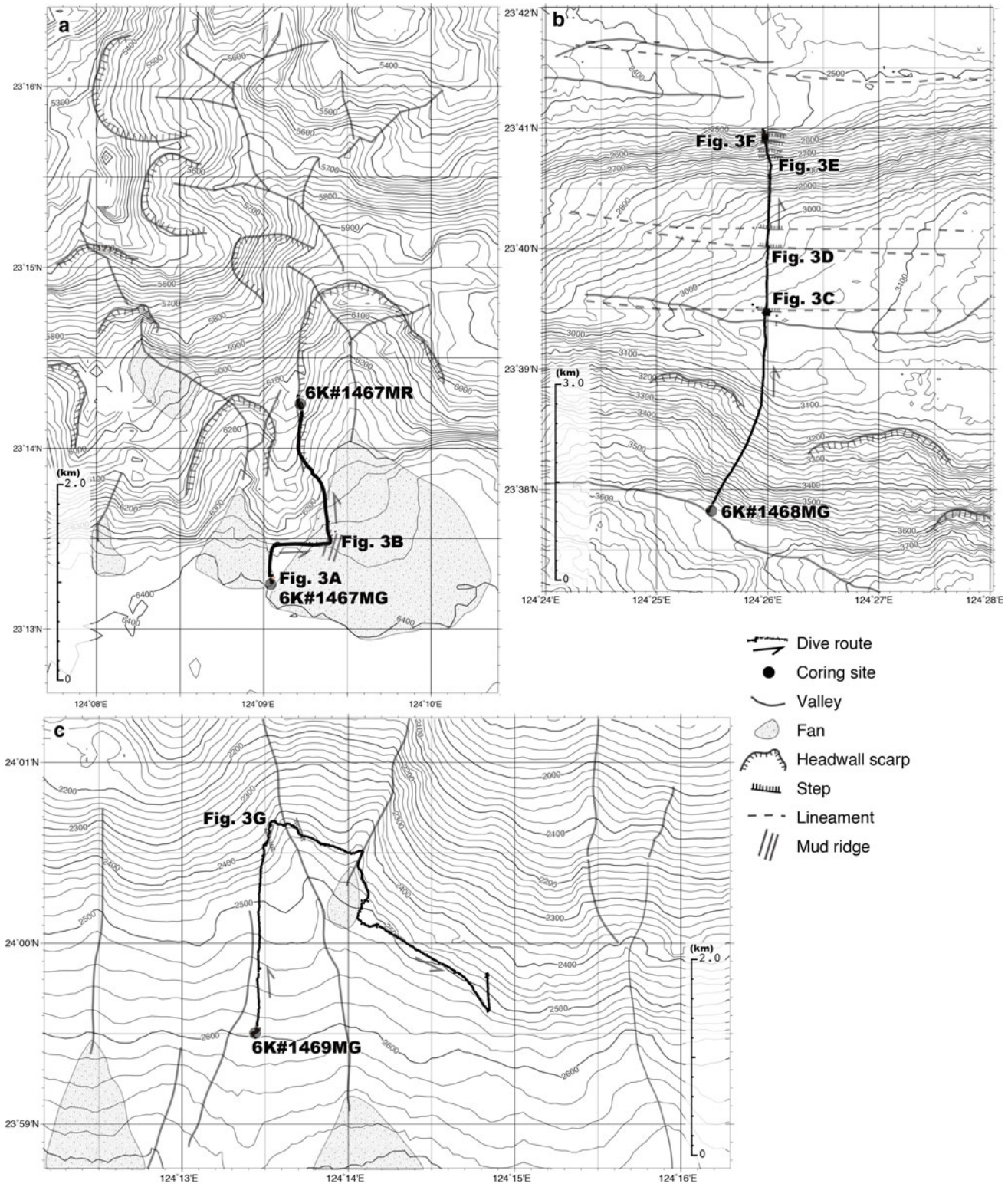

Fig. 3 Detailed bathymetry in the dive survey areas: **a** 6K#1467, **b** 6K#1468, and **c** 6K#1469

using the Monterey Bay and Aquarium Research Institute (MBARI) type corer. At 6160 m water depth, we discovered an outcrop comprising of three horizontal brown sediment layers each of which measured ∼ 20 cm in thickness. At 6115 m water depth, we collected a sediment core sample from the landward trench slope (sample 6 K#1467MR) using an MBARI corer, following which we left the seafloor at 6093 m water depth (Figs. 3 and 4).

Survey 6K#1468 was conducted on 2 September 2016. We landed on the seafloor at a depth of 3653 m at a site located at the foot of a cliff that might represent a lateral wall of submarine channel and/or headwall scar of the submarine slide that generated the 1771 Meiwa tsunami (Okamura et al. 2018). The slope extends over a distance of ∼ 1.8 km from ∼ 3600 to ∼ 3100 m water depth. The entire slope is covered with thick sediment, with no apparent faults, microbial mats, or colonies of chemosynthetic organisms. On the gentle slope extending from ∼ 3100 to 2900 m water depth, we observed several fault-related cliffs oriented mostly E–W and small outcrops of layered sedimentary rocks. The slope from ∼ 2900 to 2500 m water depth was not covered by fresh soft sediment, but instead comprised of partially hardened mud rocks at the seafloor (Figs. 3 and 4).

Survey 6K#1469 was performed on 3 September 2016. We landed at a water depth of about 2600 m, where the seafloor was flat and gray-colored, with several small dunes. We observed a step oriented NNE–SSW, which might represent the western wall of a shallow channel. The step has a relief of ∼ 1.0–1.5 m and exposes two units of strata. Farther eastward, we observed the western wall of the channel (Figs. 3 and 4).

4 Descriptions of Core Samples

Core sample 6K#1467MG was 35.5 cm long and was collected at 23°13.3014′N, 124°9.0358′E in 6371 m of water depth (Fig. 3). This core is composed of dark-olive-gray (2.5Y3/1) ashy silty clay throughout. The clay contains interbeds of fine- to medium-grained sand at 4, 8.4, 12, 14, 22, and 27 cm in core depth. A dark-olive-black (7.5Y2/2) silty clay layer was observed at 5–6 cm, and a yellowish-olive-black (10Y3/2) clay at 13.0–13.5 cm (Fig. 5).

Core sample 6K#1467MR was a length of 37 cm and was collected from a gentle slope with a thick cover of soft mud at 23°14.2477′ N, 124° 9.2242′ E in 6115 m of water depth (Fig. 3). This core is composed of olive-black (7.5Y3/1) ashy clayey silt throughout. The clayey silt is massive above 16 cm and is interbedded with darker-colored laminae below 16 cm. An olive-black (5Y3/1) clay layer (2 mm thick) occurs at 20 cm (Fig. 5). The bedding planes in this core have a dip of 5–10°, as discovered during vertical penetration by the corer.

Core sample 6K#1468MG was 38 cm long and was collected at 23° 37.8476′ N, 124° 25.4856′ E in 3653 m of water depth (Fig. 3). The sampling site is characterized by mud on a flat seafloor with small mounds of about 20 km in diameter. The core sample is yellowish gray (2.5Y4/1) at 0–6 cm, gradually becoming darker at 6–12 cm, dark grayish yellow (2.5Y4/2) at 12–35 cm, and brownish black (2.5Y3/2) at 35–38 cm (Fig. 5).

Core sample 6 K#1469MR was 26 cm long and was collected at 23° 59.5252′ N, 124° 13.4547′ E in 2583 m of water depth (Fig. 3). The seafloor at the sampling site is characterized by a flat floor with small white mounds (10–15 cm in diameter). The core sample is composed of bioturbated calcareous ooze, with numerous planktonic foraminifers and calcareous nannofossils throughout. The core color changes gradually with depth, being dark olive (5Y4/3) at 0–24 cm as a brownish surface oxidized layer, and dark olive gray (2.5Y3/1) at 24–39 cm as a grayish anoxic layer. The color at the boundary between these two layers is lighter than the grayish layer at 18–22 cm and is pale gray at 24–30 cm (Fig. 5).

5 Methods

5.1 Natural Gamma Radiation and Gamma-Ray Densitometry

In order to detect chemical characteristics of lamina, Natural gamma radiation (NGR) and gamma-ray attenuation (GRA) bulk densities were measured over 2 cm intervals using a multisensor core logger (MSCL). Here, we briefly explain these measurement methods, details of which can be found in Blum (1997).

Potassium (^{40}K), thorium (^{232}Th), and uranium (^{238}U) are radioisotopes that have a sufficiently long decay life to produce an appreciable amount of gamma rays. Minerals that fix K, U, and Th, such as clay minerals, are the principal source of NGR. Other sources include arkosic silts and sandstones, potassium salts, bituminous and alunitic schists, phosphates, certain carbonates, some coals, and felsic or mafic igneous rocks.

The bulk density of sediments and rocks is estimated from the measurement of GRA. GRA data can provide a precise and densely sampled record of bulk density, which is an indicator of changes in lithology and porosity. GRA records are frequently used for core-to-core correlation. Another important application of GRA measurements is the calculation of acoustic impedance and the construction of synthetic seismograms.

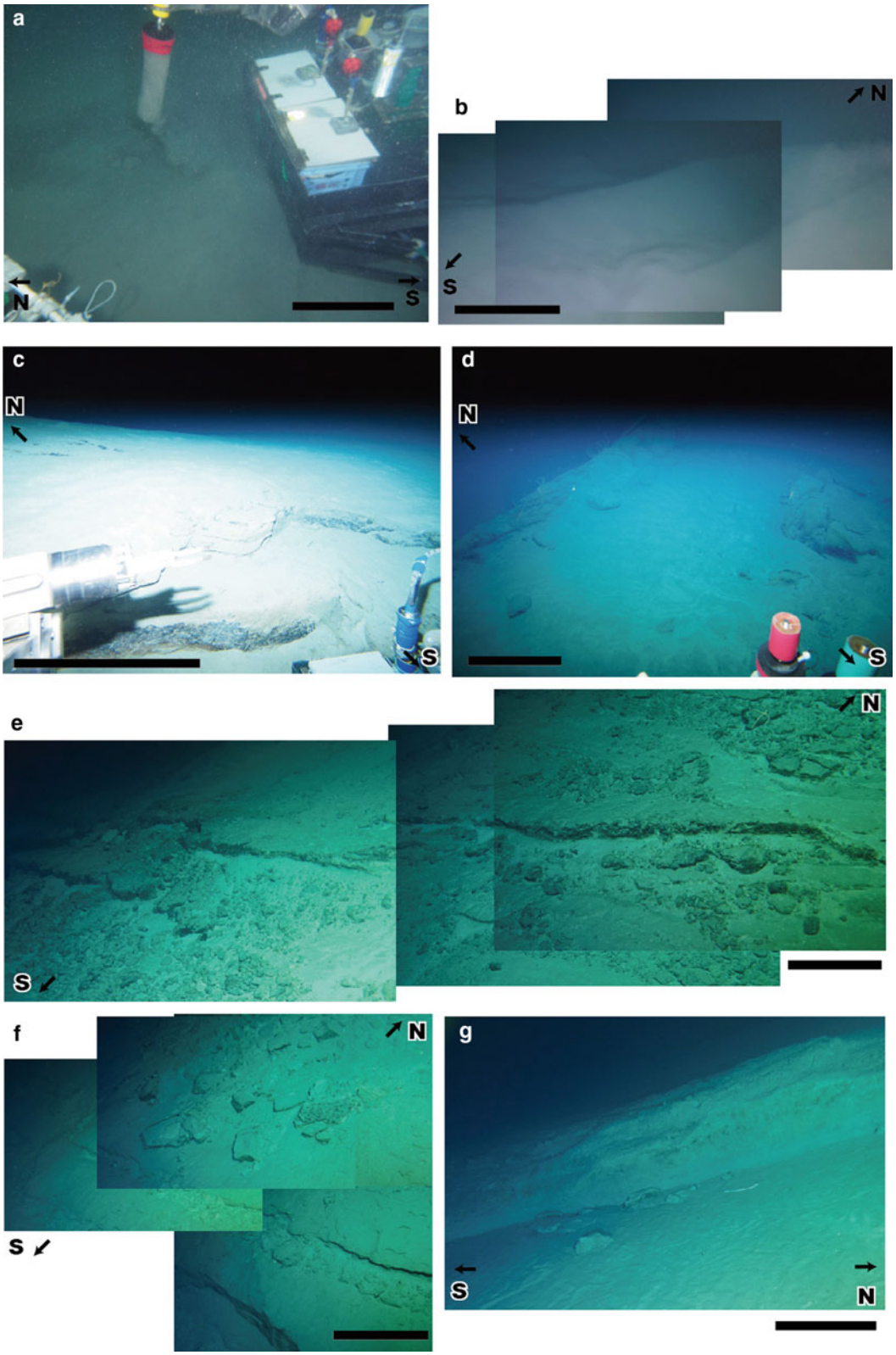

Fig. 4 Photographs taken during the dive surveys. The locations of the photographs are shown in Fig. 3. A: Sediment core collected from muddy seafloor in the Ryukyu Trench, 6K#1467. B: Parting lineations on a deep-sea fan in the Ryukyu Trench, 6K#1467. C: An E–W step with a height of ~ 1 m, 6K#1468. D: An E–W step with a height of ~ 0.5 m, 6K#1468. E: An E–W headwall scarp with a height of ~ 0.5 m and mudstone blocks measuring several centimeters in diameter, 6K#1468. F: An E–W headwall scarp with a height of ~ 0.5 m high and mudstone blocks measuring several centimeters in diameter, 6K#1468 and G: Lateral wall with a height of ~ 1 m high along a valley, 6K#1469

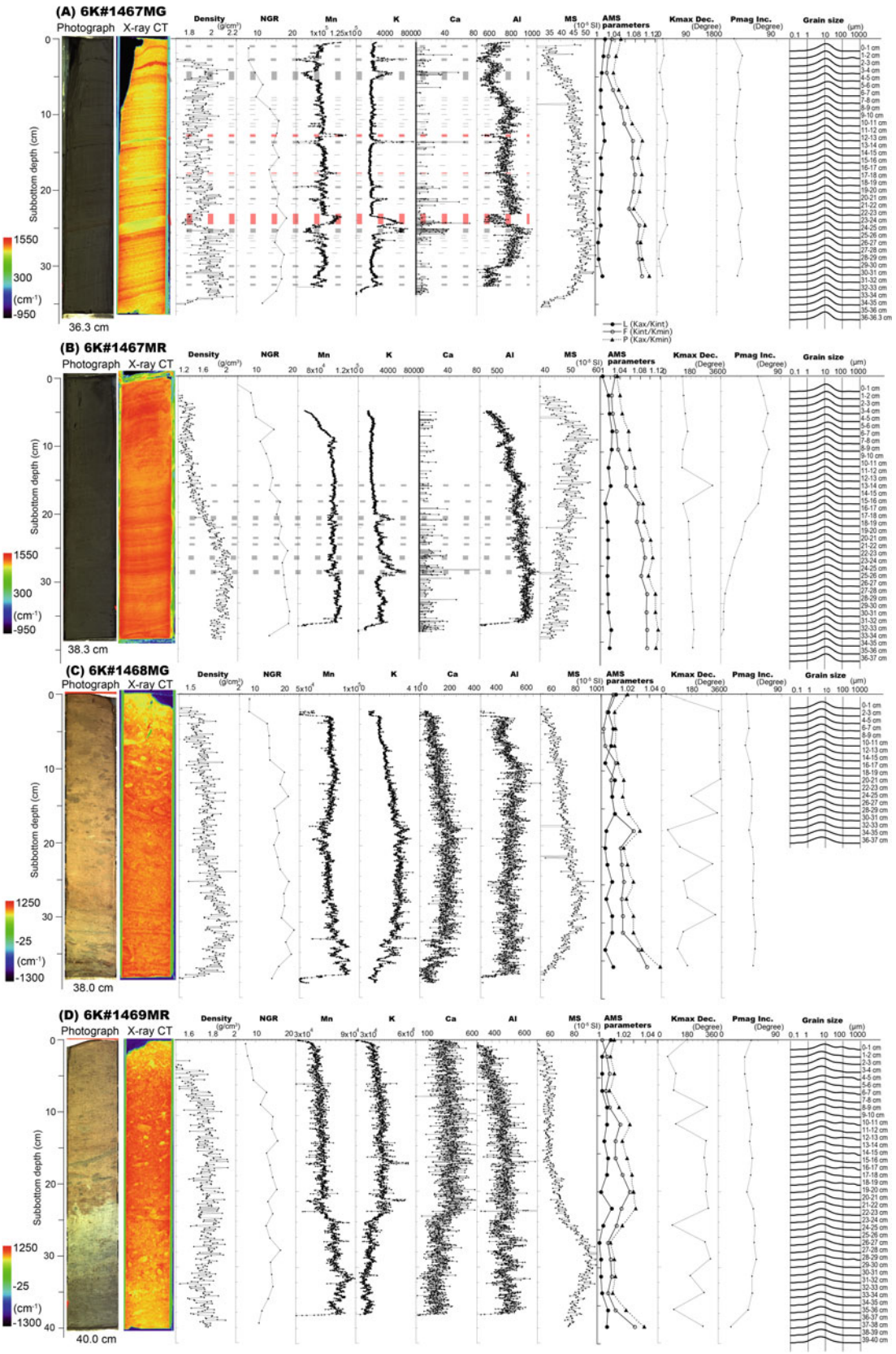

Fig. 5 Core samples profiles: **a** 6K#1467MG, **b** 6K#1467MR, **c** 6K#1468MG, and **d** 6K#1469MR. Columns (from left to right) are core photograph, X-ray CT image, density measured by gamma-ray attenuation (GRA), natural gamma ray (NGR), representative ITRAX element profiles (Mn, K, Ca, and Al), magnetic susceptibility (MS), AMS parameters (P, F, and L), K_{max} declination (K_{max} Dec.), paleomagnetic inclination (Pmag Inc.), and grain size distribution

5.2 Grain Size Determinations

Grain size distributions were determined using a Mastersizer laser diffraction grain size analyzer (Sysmex Co. Ltd.). Approximately 0.1 g of wet sediment sampled at a 1 cm interval (2 cm interval for 6K#1468MG) was disaggregated in boiling water in a glass beaker and then left for 24 h. Each sample was further disaggregated by ultrasonic treatment for 30–60 s just before measurement.

5.3 Analysis of Element Contents

Element profiles were measured on the split face of the core samples using an ITRAX XRF core scanner (Cox Analytical Systems). First, a flat surface was made on each core sample, following which element contents were measured at 0.2 mm intervals, for 10 s at each point. The analytical conditions of the scanner were 30 kV and 55 mA.

5.4 $^{210}Pb_{ex}$ measurements

^{210}Pb is a natural radionuclide of the uranium decay series and has a half-life of 22.3 year. In sediments, ^{210}Pb originates from (1) the decay reaction of ^{226}Ra within the mineral matrix (supported fraction), and (2) the adsorption of ^{210}Pb atoms onto the surfaces of particles, derived from the decay of ^{222}Rn in the water column or from the atmosphere (unsupported fraction) (Koide et al. 1972). Unsupported ^{210}Pb, also termed excess ^{210}Pb or $^{210}Pb_{ex}$, can be used to determine mass accumulation rates over a time scale of about 100 year (e.g., Nittrouer et al. 1979). ^{137}Cs (half-life of 30 year) is an artificial radionuclide dispersed into the natural environment mainly by nuclear bomb tests after 1953. The maximum ^{137}Cs fallout was recorded in 1963, with fallout levels decreasing after the cessation of atmospheric nuclear bomb tests. In the marine environment, ^{137}Cs has been supplied both by atmospheric fallout and by sediments discharged by rivers (Smith and Ellis 1982; Ritchie and McHenry 1990). Since ^{137}Cs is used as a chronological tracer, ^{137}Cs profiles in sediment are commonly used in conjunction with $^{210}Pb_{ex}$ profiles to determine sediment accumulation rates (e.g., Baskaran and Naidu 1995; Kato et al. 2003).

5.5 Magnetic Fabric Analyses

To obtain an indication of the sedimentary fabric, we measured the anisotropy of magnetic susceptibility (AMS) using an AGICO KLY-4S anisotropy magnetic susceptometer. Test specimens were encased in plastic cubes with a volume of 7 cm^3. The resultant measurement interval through the cores was therefore $\sim$ 1.9 cm. The obtained AMS values are represented by magnetic ellipsoids, of which the maximum, intermediate, and minimum axes are denoted by K_{max}, K_{int}, K_{min}, respectively. In general, the magnetic ellipsoid indicates the degree of alignment of magnetic particles in sediments (i.e., the magnetic fabric; Tarling and Hrouda, 1993). In this study, we used the following parameters: P (degree of anisotropy) = K_{max}/K_{min}, F (degree of foliation) = K_{int}/K_{min}, and L (degree of lineation) = K_{max}/K_{int}.

Paleomagnetism was measured on the same AMS plastic cube samples and using a superconductive magnetometer (2G-Enterprises, CA, US). We conducted step-wise alternating-field demagnetization during measurements of paleomagnetism. Since declination data are gradually shifted downward due to twisting to twisting during coring, magnetic north was corrected accordingly using the least-square method to reconstruct the in situ north direction of the core.

6 Results

6.1 Physical Properties and Grain Size Distribution

Core-sample density values based on the GRA measurements range from 1.2 to 2.0 g/cm^3 (Fig. 5). In the uppermost 4–5 cm, density values are mostly 1.5–1.6 g/cm^3, reflecting a high water content. Density values increase gradually with burial depth, reflecting burial consolidation. NGR counts increase with burial depth because of the increase in radioactive nuclei in a given sample volume with increasing burial consolidation.

Grain size distributions show a peak at $\sim$ 10 μm diameter in cores 6K#1467MG and 6K#1467MR. Due to the presence of laminae, sand-sized particles are found in several horizons in the core sediments. Grain size distributions show mostly silty clay with peaks at $\sim$ 5–10 μm diameter in cores 6 K#1468MG and 6K#1469MR. In these cores, the grain size of sediment in the shallow horizons ($<\sim$ 5 cm deep) is larger than that in the deeper horizons ($>\sim$ 20 cm deep).

6.2 Element Profiles

We measured 56 elements, of which four representative element (Mn, K, Ca, and Al) profiles are presented in Fig. 5. These profiles enabled two types of parallel bands to be identified in cores 6K#1467MG and 6K#1467MR. One type is low-Computed Tomography (CT)-value bands, which are

characterized by high Mn and K, and low Ca and Al values, as depicted by broken red lines (three lines for sample 6 K#1467MG) in Fig. 5a. The other type is high-CT-value bands, which are characterized by low Mn, high K, relatively high Ca, and moderate Al values, as shown by broken gray lines (28 lines for sample 6K#1467MG and 8 lines for 6K#1467MR) in Fig. 5a, b.

6.3 $^{210}Pb_{ex}$ Measurements

$^{210}Pb_{ex}$ concentrations measured in the sediments and a depth for sample 6K#1467MG were presented in Fig. 6 and Table 1. The $^{210}Pb_{ex}$ concentration was ~ 666 Bq/kg at 0–1 cm depth and gradually decreased with increasing burial depth to ~ 200 Bq/kg at 7–8 cm depth. The trend in $^{210}Pb_{ex}$ concentration showed a constant exponential decline with burial depth without any vertical mixing related to bioturbation. The absence of significant sediment mixing was also supported by X-ray CT images (Fig. 5b).

6.4 Magnetic Fabrics

Most of the magnetic susceptibility values in the studied cores lie between 0.1×10^{-3} and 1.5×10^{-3} SI units. There are sharp peaks in the range of ~ $2.0–3.0 \times 10^{-3}$ SI units in silt layers (Fig. 5).

Paleomagnetic directions in all of the core samples were mostly stable from 50 to 800 G during the stepwise alteration of field demagnetization. In this study, we used declination and inclination data under 200 G conditions. Paleomagnetic inclinations are mostly 40–50° downward for the Brunhes chron, but those of 6K#1467MR vary from 70 to 5° downward.

The magnetic susceptibility of the samples is $4–9 \times 10^{-4}$ SI throughout the cores (Fig. 5). This range reflects differences in the content, type, and/or amount of magnetic mineral grains. Following Tarling and Hrouda (1993), the magnetic minerals contributing to the magnetic susceptibility and its anisotropy in our samples were assumed to be ferrimagnetic and paramagnetic mineral grains.

Values of P, F, and L for samples 6K#1468MG and 6K#1469MR are mostly 1.02 throughout the cores (Fig. 5). These values indicate that the magnetic mineral grains are arranged with a low degree of preferred orientation (almost random) in the sediment, most likely as a result of intense bioturbation. In contrast, values of P and F in 6K#1467MG and 6K#1467MR change from 1.03 to 1.10 downward, but L values are low throughout the cores (Fig. 5). This pattern of values shows that the magnetic mineral grains are arranged with a strong preferred orientation, most likely as a result of the parallel laminae in the core sediments.

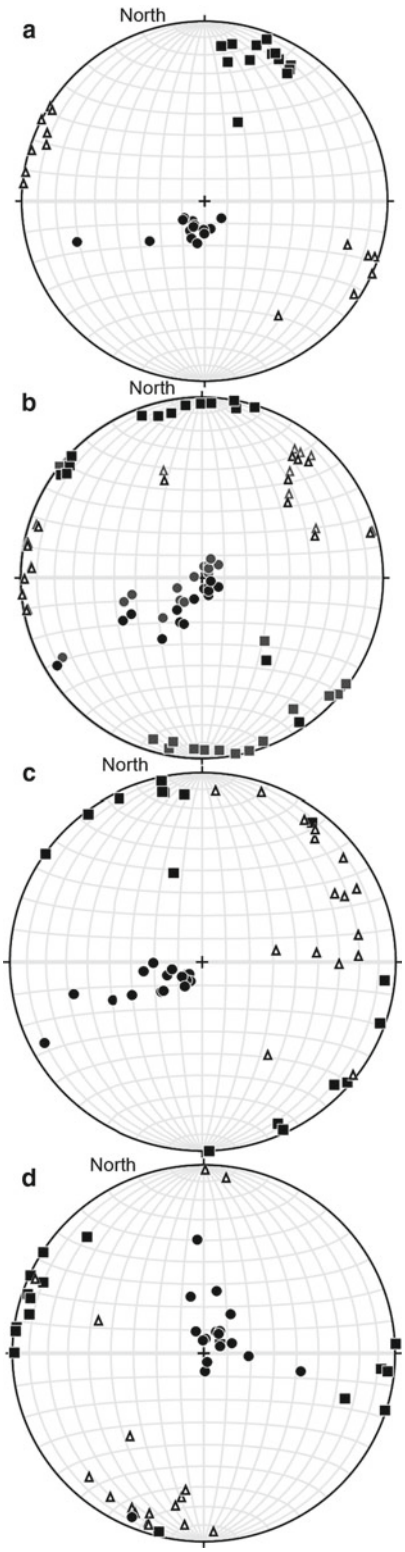

Fig. 6 Lower-hemisphere stereoplots of K_{max} (solid squares), K_{int} (open triangles), and K_{min} (solid circles) for core samples **a** 6K#1467MG, **b** 6K#1467MR, **c** 6K#1468MG, and **d** 6 K#1469MR. In (**b**), gray points indicate original data, and black points depict data that were rotated mostly parallel to a slope of about 10° tilted southward

Table 1 $^{210}Pb_{ex}$ profile data for sample 6K#1467MG

Depth (cm)	excessPb (Bq/kg)
0–1	666.1 ± 11.2
1–2	555.9 ± 8.5
2–3	388.8 ± 5.6
4–5	296.6±5.0
7–8	204.2±3.9

7 Discussion

As mentioned above, core samples 6K#1467MG and 6K#1467MR are characterized by two types of sediment bands. One is three low-CT value bands of clay layers, and the other is high-CT-value of sandy and silty laminae. The total number of laminae can be counted 28 sandy and silty laminae using element profiles as shown in Fig. 5. The sedimentary grains in the thick laminae could be supplied from a shallower slope than the carbonate compensate depth, because these consist of relative high Ca at 5, 15, 22, and 25 cm deep. In contrast to these thick laminae, thin laminae without high Ca might be formed by sedimentary grains supplied from a slope area directly above the trench floor.

7.1 Paleocurrent Analysis of the Core Samples

We used paleomagnetic north directions in each core under 200 G AF demagnetization conditions because these measurements are stable. We corrected the K_{max} directions of the AMS using paleomagnetic north in each core following the method of Kawamura et al. (2002). The corrected data, magnetic susceptibilities, and AMS data for each core are illustrated in Fig. 6 with respect to present-day north as a reference frame.

The corrected K_{max} directions show some consistency (Fig. 6). K_{max} directions are concentrated along NW–SW for 6K#1468MR and WNW–ESE for 6K#1469MR, and are sub-parallel to the slope direction, whereas those for 6K#1467MG dip to the south at $\leq$ 10°, suggesting imbrication of the sedimentary grains.

In contrast, K_{max} directions for sample 6K#1467MR dip south at $\sim$ 5° and paleomagnetic inclinations are 40–50° downward, whereas the inclinations of sample 6K#1467MR are shallower with increasing burial depth owing to the downslope gradient of the bedding plane. Therefore, we tilted the dataset of 6K#1467MR by 10° southward to adjust for the downslope gradient. As a result, the post-rotation plots are similar to those for 6K#1467MG (Fig. 6b).

According to Kawamura et al. (2002), the paleocurrent directions for 6K#1467MG and 6K#1467MR can be interpreted as indicating flow from north to south.

7.2 Mass Accumulation Rates on the Trench Floor

Figure 7 presents a $^{210}Pb_{ex}$ profile for sample 6K#1467MG. The cumulative mass for $^{210}Pb_{ex}$ was calculated as:

$$W = \int \rho r dD$$

where W is the cumulative mass of sediment (g/cm^2), ρ is the dry bulk density of the sediment (g/cm^3), and D is the depth from the top of the core (cm).

Mass accumulation rates were calculated from the $^{210}Pb_{ex}$ profile (Fig. 7). To consider compaction of the sediment buried, the mass accumulation rate was expressed in g/cm^2/year using $^{210}Pb_{ex}$ concentration and cumulative mass (g/cm^2). For sample 6 K#1467MG, exponential mass accumulation curves were fitted (Koide et al. 1972). The calculated mass accumulation rate was 2.42 g/cm^2/year.

7.3 Submarine Sliding at the Toe of the Ryukyu Accretionary Prism

The paleocurrent direction of the laminated sediments is estimated to have been from north to south, indicating that

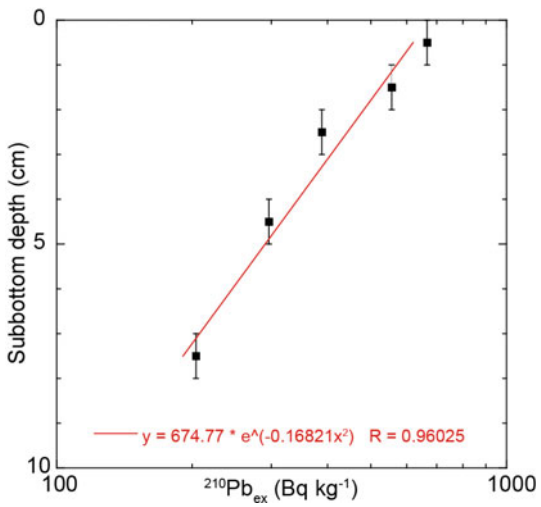

Fig. 7 $^{210}Pb_{ex}$ profile for sample 6K#1467MG

the sediments were not transported along the trench but rather from the landward slope, probably from repeated submarine slides. The mean sedimentation rate for 6K#1467MG was calculated at 2.42 mm/year using $^{210}Pb_{ex}$ concentration measurements and an age for the 10 cm horizon of roughly 50 year ago. Using the estimated sedimentation rate and the total number of laminae detected using element profiles within 10 cm deep (8 laminae as shown in Fig. 5), we simply calculated that the recurrence interval of the silt/sand layers is typically ~ 6 year for sample 6K#1467MG. These results indicate that repeated ~ 6-year-interval submarine slides have occurred continuously at the toe of the landward trench slope in the Ryukyu Trench over the last ~ 50 year, suggesting that the toe of the accretionary wedge is in a continually unstable state with respect to the triggering of submarine slides.

8 Summary

(1) We performed three dive surveys using the 6K manned submersible in the Ryukyu Trench. These dive sites were near a large submarine slide that generated the AD 1771 Meiwa tsunami.
(2) Dive site 6K#1468 was on the uppermost part of the submarine slide, where recent steps and fissures were observed. Dive site 6K#1467 was located at the toe of the submarine slide, which was covered by a muddy sediment layer. No chemosynthetic biocommunities were observed. Core sample 6K#1467MG comprised muddy sediments interlayered with silt and/or sand laminations.
(3) The paleocurrent direction of the laminated sediments was from north to south, indicating that the sediments were not transported along the trench but rather from the landward slope, probably as a result of the occurrence of repeated small submarine slides.
(4) The sedimentation rate for core sample 6K#1467MG was calculated as 2.42 mm/year by $^{210}Pb_{ex}$ measurements through the core and an age for the 10 cm horizon of ~ 50 year ago.
(5) We infer that small submarine slides repeated at an interval of ~ 6 year have occurred persistently at the toe of the landward trench slope in the Ryukyu Trench during the last ~ 50 year.

Acknowledgements We thank the captains, crew, shipboard scientists, and operation teams of the *Shinkai 6500* submersible during the YK16-11 cruise. The authors gratefully acknowledge Y. Yamamoto (Kochi University) for help with the measurement of magnetic properties, and M. Murayama, G. Uramoto, and T. Matsuzaki (Kochi University) for grain-size analyses. This study was performed under the cooperative research programs of the Institute of Nature and Environmental Technology, Kanazawa University (Acceptance No. 18026) and the Center for Advanced Marine Core Research (CMCR), Kochi University (17B062).

References

Abe K (1979) Size of great earthquakes of 1837–1974 inferred from tsunami data. J Geophys Res 84:1561–1568. https://doi.org/10.1029/JB084iB04p01561

Araoka D, Yokoyama Y, Suzuki A, Goto K, Miyagi K, Miyazawa K, Matsuzaki H, Kawahata H (2013) Tsunami recurrence revealed by *Porites* coral boulders in the southern Ryukyu Islands, Japan. Geology 41:919–922. https://doi.org/10.1130/G34415.1

Baskaran M, Naidu AS (1995) ^{210}Pb-derived chronology and the fluxes of ^{210}Pb and ^{137}Cs isotopes into continental shelf sediments, East Chukchi Sea Alaskan Arctic. Geochimica et Cosmochimica Acta 59(21):4435–4448. https://doi.org/10.1016/0016-7037(95)00248-X

Blum P (1997) Physical properties handbook: a guide to the shipboard measurement of physical properties of deep-sea cores. ODP Tech Note 26.https://doi.org/10.2973/odp.tn.26.1997

Fryer GJ, Watts P, Pratson LF (2004) Source of the great tsunami of 1 April 1946: a landslide in the upper Aleutian forearc. Mar Geol 203:201–218. https://doi.org/10.1016/S0025-3227(03)00305-0

Goto K, Kawana T, Imamura F (2010) Historical and geological evidence of boulders deposited by tsunamis, southern Ryukyu Islands, Japan. Earth-Sci Rev 102:77–99. https://doi.org/10.1016/j.earscirev.2010.06.005

Goto K, Shimabukuro A (2012) The 1771 Meiwa tsunami revealing by multidisciplinary researches. Kagaku, 82, 208–214 (in Japanese)

Gracia E, Danobeitia J, Verges J, PARSIFAL Team (2003) Mapping active faults offshore Portugal (36°N–38°N): Implications for seismic hazard assessment along the southwest Iberian margin. Geology 31(1):83–86.https://doi.org/10.1130/0091-7613(2003)031<0083:MAFOPN>2.0.CO;2

Hisamitsu A, Goto K, Imamura F (2014) Local paleo-tsunami size evaluation using numerical modeling for boulder transport at Ishigaki Island Japan. Episodes 37(4):265–276. https://doi.org/10.18814/epiiugs/2014/v37i4/006

Hornbach MJ, Braudy N, Briggs RW, Cormier M-H, Davis MB, Diebold JB, Dieudonne N, Douilly R, Frohlich C, Gulick SPS, Johnson HE III, Mann P, McHugh C, Ryan-Mishkin K, Symithe SJ, Taylor FW, Templeton J (2010) High tsunami frequency as a result of combined strike-slip faulting and coastal landslides. Nat Geosci 3:783–788. https://doi.org/10.1038/ngeo975

Kanamori H (1972) Mechanism of tsunami earthquakes. Phys Earth Planet Inter 6:346–359. https://doi.org/10.1016/0031-9201(72)90058-1

Kanamori H, Kikuchi M (1993) The 1992 Nicaragua earthquake: a slow tsunami earthquake associated with subducted sediments. Nature 361:714–716. https://doi.org/10.1038/361714a0

Kato Y, Kitazato H, Shimanaga M, Nakatsuka T, Shirayama Y, Masuzawa T (2003) ^{210}Pb and ^{137}Cs in sediments from Sagami Bay, Japan: sedimentation rates and inventories. Prog Oceanogr 57:77–95. https://doi.org/10.1016/S0079-6611(03)00052-1

Kawamura K (2020) Submarine slides and tsunamis 1. Introduction for the lectures. Geotech Eng Mag 68(4):29–30 (in Japanese)

Kawamura K, Kanamatsu T, Yamada Y (2017) Submarine slides and marine geohazards: the study results so far and current problems. J Geol Soc Jpn 123(12):999–1014 (Japanese with English abstract). https://doi.org/10.5575/geosoc.2017.0031

Kawamura K, Laberg JS, Kanamatsu T (2014) Potential tsunamigenic submarine landslides in active margins. Mar Geol 356:44–49. https://doi.org/10.1016/j.margeo.2014.03.007

Kawamura K, Ogawa Y, Anma R, Yokoyama S, Kawakami S, Dilek Y, Moore GF, Hirano S, Yamaguchi A, Sasaki T, YK05-08 Leg 2, YK06-02 Shipboard Scientific Parties (2009) Structural architecture and active deformation of the Nankai accretionary prism, Japan: submersible survey results from the Tenryu submarine canyon. Geol Soc Am Bull 121:1629–1646.https://doi.org/10.1130/B26219.1

Kawamura K, Sasaki T, Kanamatsu T, Sakaguchi A, Ogawa Y (2012) Large submarine landslides in the Japan Trench: a new scenario for additional tsunami generation. Geophys Res Lett 39:L05308. https://doi.org/10.1029/2011GL050661

Kawata Y, Benson BC, Borrero JL, Davies HL, deLange WP, Imamura F, Letz H, Nott J, Synolakis C (1999) Tsunami in Papua New Guinea was as intense as first thought. Eos Transaction AGU 80(9):101–112. https://doi.org/10.1029/99EO00065

Kawamura K, Ikehara K, Kanamatsu T, Fujioka K (2002) Paleocurrent analysis of turbidites in Parece vela Basin using anisotropy of magnetic susceptibility. Journal of the Geological Society of Japan 108(4):207–218. https://doi.org/10.5575/geosoc.108.207

Koide M, Soutar A, Goldberg ED (1972) Marine geochemistry with ^{210}Pb. Earth Planet Sci Lett 14:442–446. https://doi.org/10.1016/0012-821X(72)90146-X

Nakamura M (2009) Fault model of the 1771 Yaeyama earthquake along the Ryukyu Trench estimated from the devastating tsunami. Geophys Res Lett 36:L19307. https://doi.org/10.1029/2009GL039730

Newman AV, Okal EA (1998) Sandaun earthquake as studied by teleseismic energy. Eos Transaction AGU 79(45):F564

Nittrouer CA, Sternberg RW, Carpenter R, Bennett JT (1979) The use of Pb-210 geochronology as a sedimentological tool: application to the Washington continental shelf. Mar Geol 31(3/4):297–316. https://doi.org/10.1016/0025-3227(79)90039-2

Okamura Y, Nishizawa A, Fujii Y, Yanagisawa H (2018) Accretionary prism collapse: a new hypothesis on the source of the 1771 giant tsunami in the Ryukyu Arc SW Japan. Sci Rep 8:13620. https://doi.org/10.1038/s41598-018-31956-8

Plafker G, Mayo LR (1965) Tectonic deformation, subaqueous slides and destructive waves associated with the Alaskan March 27, 1964 earthquake; an interim geologic evaluation. United States Department of the Interior Geological Survey Open-file report, USGS, 19p. https://doi.org/10.3133/ofr65124

Ritchie JC, McHenry JR (1990) Application of radioactive fallout cesium-137 for measuring soil erosion and sediment accumulation rates and patterns: a review. J Environ Qual 19(2):215–233. https://doi.org/10.2134/jeq1990.00472425001900020006x

Sassa S, Takagawa T (2019) Liquefied gravity flow-induced tsunami; first evidence and comparison from the 2018 Indonesia Sulawesi earthquake and tsunami disasters. Landslides 16:195–200. https://doi.org/10.1007/s10346-018-1114-x

Seno T (2005) Plate motions in the world. J Geogr 114(3):350–366 (in Japanese with English abstract). https://doi.org/10.5026/jgeography.114.3_350

Smith JN, Ellis KM (1982) Transport mechanism for Pb-210, Cs-137 and Pu fallout radionuclides through fluvial–marine systems. Geochim Cosmochim Acta 46:941–954. https://doi.org/10.1016/0016-7037(82)90050-3

Tanioka Y, Satake K (1996) Tsunami generation by horizontal displacement of ocean bottom. Geophys Res Lett 23:861–864. https://doi.org/10.1029/96GL00736

Tanioka Y, Seno T (2001) Sediment effect on tsunami generation of the 1896 Sanriku tsunami earthquake. Geophys Res Lett 28:3389–3392. https://doi.org/10.1029/2001GL013149

Tappin DR, Watts P, McMurtry GM, Lafoy Y, Matsumoto T (2001) The Sissano, Papua New Guinea tsunami of July 1998—offshore evidence on the source mechanism. Mar Geol 175:1–23. https://doi.org/10.1016/S0025-3227(01)00131-1

Tappin DR, Watts P, Grilli ST (2008) The Papua New Guinea tsunami of 17 July 1998: anatomy of a catastrophic event. Nat Hazard 8:243–266. https://doi.org/10.5194/nhess-8-243-2008